

# TROPOMI NO<sub>2</sub> in the United States: A detailed look at the annual averages, weekly cycles, effects of temperature, and correlation with PM<sub>2.5</sub>

Daniel L. Goldberg<sup>1</sup>, Susan Anenberg<sup>2</sup>, Arash Mohegh<sup>1</sup>, Zifeng Lu<sup>3</sup>, and David G. Streets<sup>3</sup>

<sup>1</sup>George Washington University

<sup>2</sup>george washington university

<sup>3</sup>Argonne National Laboratory (DOE)

November 26, 2022

## Abstract

Observing the spatial heterogeneities of NO<sub>2</sub> air pollution is an important first step in quantifying NO<sub>x</sub> emissions and exposures. This study investigates the capabilities of the Tropospheric Monitoring Instrument (TROPOMI) in observing the spatial and temporal patterns of NO<sub>2</sub> pollution in the Continental United States (CONUS). The high instrument sensitivity can differentiate the fine-scale spatial heterogeneities in urban areas, such as hotspots related to airport/shipping operations and high traffic areas, and the relatively small emission sources in rural areas, such as power plants and mining operations. We also examine NO<sub>2</sub> columns by day-of-the-week and find that Saturday and Sunday concentrations are 16% and 24% lower respectively than during weekdays. In cities with topographic features that inhibit dispersion, such as Los Angeles, there appears to be a pollution build-up from Monday through Friday, while cities which have better dispersion have more variability during weekdays. We also analyze the correlation of temperatures and NO<sub>2</sub> column amounts and find that NO<sub>2</sub> is larger on the hottest days (>32C) as compared to warm days (26C - 32C), which is in contrast to a general decrease in NO<sub>2</sub> with increasing temperature at lower temperature bins. Finally, we compare column NO<sub>2</sub> with estimates of surface PM<sub>2.5</sub> and find fairly poor correlation, suggesting that NO<sub>2</sub> and PM<sub>2.5</sub> are becoming increasingly less correlated in CONUS. These new developments make TROPOMI NO<sub>2</sub> satellite data advantageous for policymakers and public health officials, who request information at high spatial resolution and short timescales, in order to assess, devise, and evaluate regulations.

1 **TROPOMI NO<sub>2</sub> in the United States: A detailed look at the annual averages, weekly**  
2 **cycles, effects of temperature, and correlation with PM<sub>2.5</sub>**

3  
4 Daniel L. Goldberg<sup>\*,1,2</sup>, Susan C. Anenberg<sup>1</sup>, Arash Mohegh<sup>1</sup>, Zifeng Lu<sup>2</sup>, David G. Streets<sup>2</sup>  
5  
6

7 <sup>1</sup>Department of Environmental and Occupational Health, George Washington University,  
8 Washington, DC 20052, U.S.

9 <sup>2</sup>Energy Systems Division, Argonne National Laboratory, Argonne, IL 60439, U.S.

10  
11  
12  
13  
14  
15  
16  
17 \_\_\_\_\_  
\*Corresponding author. Phone: (202)994-8102; Email: [dgoldberg@gwu.edu](mailto:dgoldberg@gwu.edu)

18

19 **Abstract**

20 Observing the spatial heterogeneities of NO<sub>2</sub> air pollution is an important first step in quantifying  
21 NO<sub>x</sub> emissions and exposures. This study investigates the capabilities of the Tropospheric  
22 Monitoring Instrument (TROPOMI) in observing the spatial and temporal patterns of NO<sub>2</sub>  
23 pollution in the Continental United States (CONUS). The high instrument sensitivity can  
24 differentiate the fine-scale spatial heterogeneities in urban areas, such as hotspots related to  
25 airport/shipping operations and high traffic areas, and the relatively small emission sources in  
26 rural areas, such as power plants and mining operations. We also examine NO<sub>2</sub> columns by day-  
27 of-the-week and find that Saturday and Sunday concentrations are 16% and 24% lower  
28 respectively than during weekdays. In cities with topographic features that inhibit dispersion,  
29 such as Los Angeles, there appears to be a pollution build-up from Monday through Friday,  
30 while cities which have better dispersion have more variability during weekdays. We also  
31 analyze the correlation of temperatures and NO<sub>2</sub> column amounts and find that NO<sub>2</sub> is larger on  
32 the hottest days (>32°C) as compared to warm days (26°C - 32°C), which is in contrast to a  
33 general decrease in NO<sub>2</sub> with increasing temperature at lower temperature bins. Finally, we  
34 compare column NO<sub>2</sub> with estimates of surface PM<sub>2.5</sub> and find fairly poor correlation, suggesting  
35 that NO<sub>2</sub> and PM<sub>2.5</sub> are becoming increasingly less correlated in CONUS. These new  
36 developments make TROPOMI NO<sub>2</sub> satellite data advantageous for policymakers and public  
37 health officials, who request information at high spatial resolution and short timescales, in order  
38 to assess, devise, and evaluate regulations.

## 39 **Introduction**

40 Enhancements of NO<sub>2</sub> serve as a stark reminder of our society's global reliance on fossil-fuel  
41 combustion. NO<sub>2</sub> – which comprises ~70% of NO<sub>x</sub> (NO<sub>x</sub> = NO + NO<sub>2</sub>) in urban airsheds (Valin  
42 et al., 2013) – primarily originates as a byproduct of fossil-fuel combustion, although there are  
43 some biogenic sources of NO<sub>2</sub> such as lightning and microbes in soil (Jacob, 2000). NO<sub>2</sub> is a  
44 toxic air pollutant, which can cause and exacerbate asthma in vulnerable populations  
45 (Achakulwisut et al., 2019; Anenberg et al., 2018) and lead to premature mortality (Burnett et al.,  
46 2004). NO<sub>2</sub> can also react in the atmosphere to create tropospheric ozone (O<sub>3</sub>), which is noted  
47 for its damaging effects including premature aging of lungs (Broeckaert et al., 1999; McConnell  
48 et al., 2002) and premature mortality (Bell, 2004; Bell et al., 2006). HNO<sub>3</sub> often represents the  
49 final chemical state of NO<sub>2</sub> in the atmosphere and when deposited, agitates the equilibrium of  
50 our ecosystems due to its acidic properties (Burns et al., 2016). NO<sub>2</sub> can also participate in a  
51 series of reactions to create particulate nitrate (NO<sub>3</sub><sup>-</sup>), a component of fine particulate matter less  
52 than 2.5 microns in diameter (PM<sub>2.5</sub>), which is the leading cause of mortality due to air pollution  
53 (Cohen et al., 2017).

54 There is a rich legacy of monitoring NO<sub>2</sub> by remote sensing instruments (Burrows et al., 1999).  
55 NO<sub>2</sub> can be observed from space because it has unique high-frequency spectral features within  
56 the 400 – 500 nm wavelength region (Vandaele et al., 1998). The newest remote sensing  
57 spectrometer, TROPOMI (VanGeffen et al., 2019; Veefkind et al., 2012), has been gathering  
58 data on the global heterogeneities of NO<sub>2</sub> air pollution since October 2017. This instrument  
59 builds on the legacy of prior Ultraviolet – Visible (UV-Vis) spectrometers including the Global  
60 Ozone Monitoring Experiment (GOME) (Burrows et al., 1999; Martin et al., 2002; Richter &  
61 Burrows, 2002), the Scanning Imaging Spectrometer for Atmospheric Cartography  
62 (SCIAMACHY) (Bovensmann et al., 1999; Heue et al., 2005), the Global Ozone Monitoring  
63 Experiment - 2 (GOME-2) instrument (Munro et al., 2016; Richter et al., 2011), and the Ozone  
64 Monitoring Instrument (OMI) (Boersma et al., 2018; Krotkov et al., 2017; Levelt et al., 2006,  
65 2018).

66 Satellite-based remote sensing instruments can be particularly useful in quantifying the trends of  
67 NO<sub>x</sub> pollution in high-emission areas (Castellanos & Boersma, 2012; Duncan et al., 2016;  
68 Georgoulias et al., 2019; Krotkov et al., 2016; McLinden et al., 2016; Stavrou et al., 2008; Van

69 Der A et al., 2008), the seasonal cycles of air pollution (Ialongo et al., 2016; Shah et al., 2020),  
70 and the weekly cycle of NO<sub>x</sub> emissions (Beirle et al., 2003; Ialongo et al., 2016; Ma et al., 2013;  
71 Russell et al., 2010; Valin et al., 2014). In an additional step, NO<sub>x</sub> emissions can be computed  
72 by combining the satellite data with meteorological information (Beirle et al., 2011, 2019; de  
73 Foy et al., 2015; Goldberg, Lu, Streets, et al., 2019; Goldberg, Saide, et al., 2019; Lorente et al.,  
74 2019; Lu et al., 2015; Valin et al., 2013) or by combining the satellite data with chemical  
75 transport models (Canty et al., 2015; Cooper et al., 2017; Qu et al., 2017; Sourì et al., 2016).  
76 Due to the consistency and robustness of the remotely-sensed NO<sub>2</sub> data record, scientists are  
77 beginning to infer information from the NO<sub>2</sub> data about other trace gases such as CO<sub>2</sub> (Goldberg,  
78 Lu, Oda, et al., 2019; Konovalov et al., 2016; Reuter et al., 2019), CH<sub>4</sub> (de Gouw et al., 2020),  
79 and CO (Lama et al., n.d.), since remotely-sensed measurements of those trace gases are  
80 generally less reliable. Therefore, remotely-sensed NO<sub>2</sub> can also be helpful in indirectly  
81 estimating greenhouse gas emissions.

82 TROPOMI's smallest pixel size ( $3.5 \times 7.2 \text{ km}^2$  at nadir, reduced to  $3.5 \times 5.6 \text{ km}^2$  at nadir on  
83 August 6, 2019) and enhanced sensitivity are significant improvements when compared to  
84 previous satellite instruments (Veefkind et al., 2012). NO<sub>2</sub> is unique due to its relatively short  
85 photochemical lifetime which varies from 2-5 h during the summer daytime (Beirle et al., 2011;  
86 de Foy et al., 2014; Laughner & Cohen, 2019; Valin et al., 2013) to 12-24 h during winter (Shah  
87 et al., 2020). As a result, tropospheric NO<sub>2</sub> concentrations are strongly correlated with local NO<sub>x</sub>  
88 emissions, which are often anthropogenic in origin.

89 Initial NO<sub>2</sub> measurements from TROPOMI show the complex spatial heterogeneities of NO<sub>2</sub>  
90 pollution with more refined resolution than any instrument before it (Griffin et al., 2019; Ialongo  
91 et al., 2020). In particular, the smaller pixel sizes aid researchers in differentiating pollution  
92 sources within a single metropolitan area such as isolating signals from airports and individual  
93 highways (Judd et al., 2019). These small-scale pixel sizes also show better agreement with the  
94 spatial features suggested by ground-based measurements (Ialongo et al., 2020; Judd et al.,  
95 2019). In particular, modeling studies have shown that matching the NO<sub>2</sub> column to 10%  
96 accuracy requires a spatial resolution of at least 4 km (Valin et al., 2011) – the approximate  
97 spatial resolution of TROPOMI. Robust high-spatial resolution estimates are also critical inputs

98 to those trying to quantify the surface-level NO<sub>2</sub> exposures (Geddes et al., 2016; Lamsal et al.,  
99 2008; Larkin et al., 2017).

100 The improved spatial resolution and instrument sensitivity also allows for shorter temporal  
101 averaging ranges (days to months) to gain the similar spatial structure it would normally take >1  
102 year to gather (Beirle et al., 2019; Dix et al., 2020; Goldberg, Lu, Streets, et al., 2019; Lorente et  
103 al., 2019). As a result, it is easier to gain insight on the short-term variations of NO<sub>x</sub> pollution  
104 when using TROPOMI, which can be especially helpful for those trying to quantify intra-annual  
105 changes in NO<sub>x</sub> emissions (F. Liu et al., 2020).

106 In this paper, we exploit TROPOMI's small pixel sizes and enhanced instrument sensitivity to  
107 analyze spatial and temporal features of NO<sub>x</sub> columns in the continental United States on annual,  
108 seasonal, weekly, and daily timescales. For example, using only a short temporal range of data,  
109 we can now answer such questions as:

- 110 • Which location within each U.S. state has the worst NO<sub>2</sub> air pollution?
- 111 • How does the NO<sub>x</sub> emissions cycle vary by day of the week?
- 112 • How does temperature affect column NO<sub>2</sub> amounts?
- 113 • What is the relative magnitude of NO<sub>2</sub> compared to PM<sub>2.5</sub>?

114 While older sensors (e.g., OMI) provided insight into some of these questions, early sensors  
115 lacked the same sensitivity and required longer oversampling times. Therefore, answers  
116 illuminated by TROPOMI provide a “clarity” that has not been seen before.

## 117 **Methods**

### 118 **TROPOMI NO<sub>2</sub>**

119 TROPOMI was launched by the European Space Agency (ESA) for the European Union's  
120 Copernicus Sentinel 5 Precursor (S5p) satellite mission on October 13, 2017. The satellite  
121 follows a sun-synchronous, low-earth (825 km) orbit with an equator overpass time of  
122 approximately 13:30 local solar time (Veefkind et al., 2012). TROPOMI measures total column  
123 amounts of several trace gases in the Ultraviolet-Visible-Near Infrared-Shortwave Infrared  
124 spectral regions (VanGeffen et al., 2019). This instrument is characterized as a passive optical  
125 satellite sensor due to its reliance on solar UV-Visible radiation to gather measurements. At

126 nadir, pixel sizes are  $3.5 \times 7 \text{ km}^2$  (reduced to  $3.5 \times 5.6 \text{ km}^2$  on August 6, 2019) with little  
127 variation in pixel sizes across the 2600 km swath. The instrument observes the swath  
128 approximately once every second and orbits the Earth in about 100 minutes, resulting in daily  
129 global coverage.

130 Using a differential optical absorption spectroscopy (DOAS) technique on the radiance  
131 measurements in the 405 – 465 nm spectral window, the top-of-atmosphere spectral radiances  
132 can be converted into slant column amounts of  $\text{NO}_2$  between the sensor and the Earth's surface  
133 (van Geffen et al., 2020). In two additional steps, the slant column quantity can be converted  
134 into a tropospheric vertical column content. In the first step, the stratospheric portion of the  
135 column (the amount above approximately 12 km in altitude) is subtracted either by using a  
136 measurement in a remote area or by using a global model estimate. In a second step, the slant  
137 tropospheric column is converted to a vertical column using a quantity known as the air mass  
138 factor. The air mass factor is the most uncertain quantity in the retrieval algorithm (Lorente et  
139 al., 2017), and is a function of the surface reflectance, the  $\text{NO}_2$  vertical profile, and scattering in  
140 the atmosphere among other factors. Using accurate and high-resolution data (spatially and  
141 temporally) as inputs in calculating the air mass factor can significantly reduce the overall errors  
142 of the air mass factor (S. Choi et al., 2019; Goldberg et al., 2017; Laughner et al., 2016, 2019;  
143 Lin et al., 2015; M. Liu et al., 2019; Russell et al., 2011; Zhao et al., 2020) and thus the  
144 tropospheric vertical column content.

145 Operationally, the TM5-MP model ( $1 \times 1^\circ$  resolution) is used to provide the  $\text{NO}_2$  vertical shape  
146 profile and the climatological Lambertian Equivalent Reflectivity ( $0.5 \times 0.5^\circ$  resolution)  
147 (Kleipool et al., 2008) is used to provide the surface reflectivities. The operational air mass  
148 factor calculation does not explicitly account for aerosol absorption effects, which are accounted  
149 for in the effective cloud radiance fraction. While the operational product does have larger  
150 uncertainties in the tropospheric column contents than a product with higher spatial resolution  
151 inputs, we limit our analysis to relative trends, which dramatically reduces this uncertainty.

## 152 **Re-gridding**

153 For our analysis we re-grid the operational TROPOMI tropospheric vertical column  $\text{NO}_2$ , with  
154 native pixels of approximately  $3.5 \times 7 \text{ km}^2$ , to a newly defined  $0.01^\circ \times 0.01^\circ$  grid (approximately  
155  $1 \times 1 \text{ km}^2$ ) centered over the continental United States (CONUS; corner points: SW:  $24.5^\circ \text{ N}$ ,

156 124.75° W; NE: 49.5° N, 66.75° W). Before re-gridding, the data are filtered so as to use only  
157 the highest quality measurements (quality assurance flag (QA\_flag) > 0.75). Once the re-  
158 gridding has been completed, the data is averaged over varying timeframes as discussed in the  
159 results section.

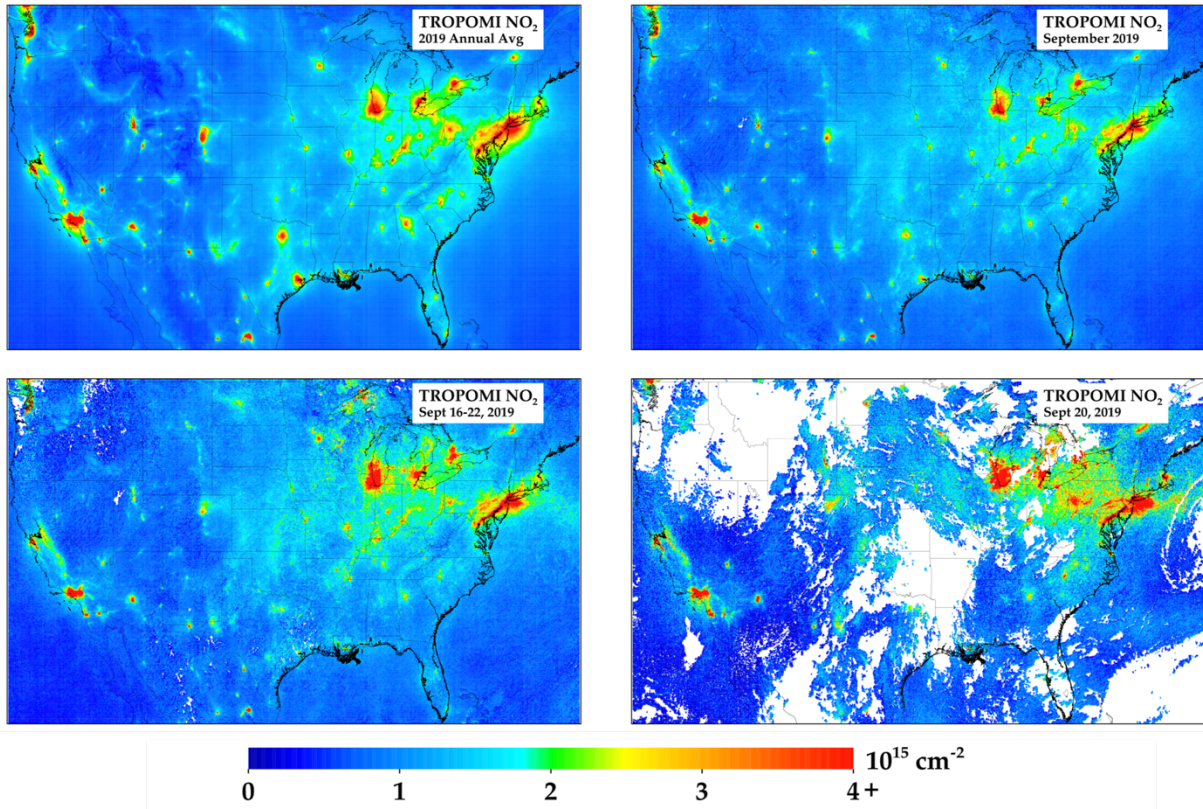
## 160 **Other Datasets**

161 Additionally, we use two complementary products in some sections of our analysis. When  
162 filtering the data based on temperature, we use the maximum daily hourly 2-meter temperature  
163 (T2m-Max) from the ERA5 re-analysis. To downscale the ERA5 re-analysis, which is provided  
164 at  $0.25^\circ \times 0.25^\circ$ , we spatially interpolate daily T2m-Max to  $0.01^\circ \times 0.01^\circ$  using bilinear  
165 interpolation. For that reason, the heat-urban island effect and any microscale meteorology  
166 features (e.g., sea breezes) will not be accounted for, but these effects should be minor for our  
167 particular analysis, which groups temperatures in  $5^\circ$  C intervals. We also compare our  $0.01^\circ \times$   
168  $0.01^\circ$  TROPOMI NO<sub>2</sub> data to an annual PM<sub>2.5</sub> dataset at the same spatial resolution  
169 (VanDonkelaar et al., 2019).

170 **Results**

171 **TROPOMI NO<sub>2</sub> in CONUS**

172 Figure 1 depicts the 2019 CONUS annual average of TROPOMI tropospheric vertical column  
173 NO<sub>2</sub> compared to averages over shorter timeframes.



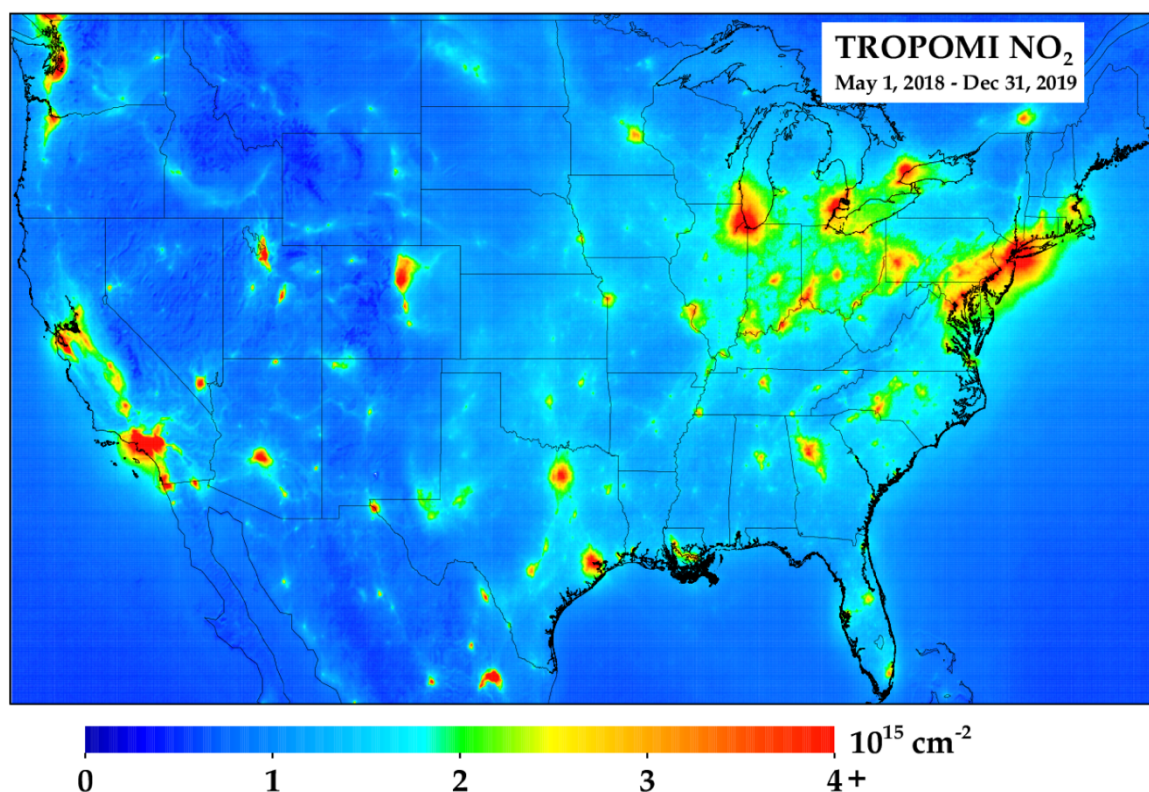
174

175 **Figure 1.** TROPOMI NO<sub>2</sub> oversampled to  $0.01^\circ \times 0.01^\circ$  spatial resolution for four different  
176 temporal resolutions: (top left) annual, (top right) monthly, (bottom left) weekly, and (bottom  
177 right) daily.

178 This example illustrates how shorter timeframes compare to the annual average in both  
179 magnitude and clarity. In the single daily snapshot (September 20, 2019), there are wide sections  
180 that are missing due to cloud coverage. In the areas that do have coverage, values can be a factor  
181 of five different than the annual average, but the spatial heterogeneities are generally captured.  
182 When oversampling over a one-week period (September 16 – 22, 2019), the image quickly starts  
183 to resemble the annual average with some differences in magnitude due to meteorological  
184 factors, such as temperature (which will be discussed later). The one-week average can therefore  
185 be considered the minimum amount of oversampling time to properly capture spatial  
186 heterogeneities. A monthly oversampled image essentially captures the same spatial

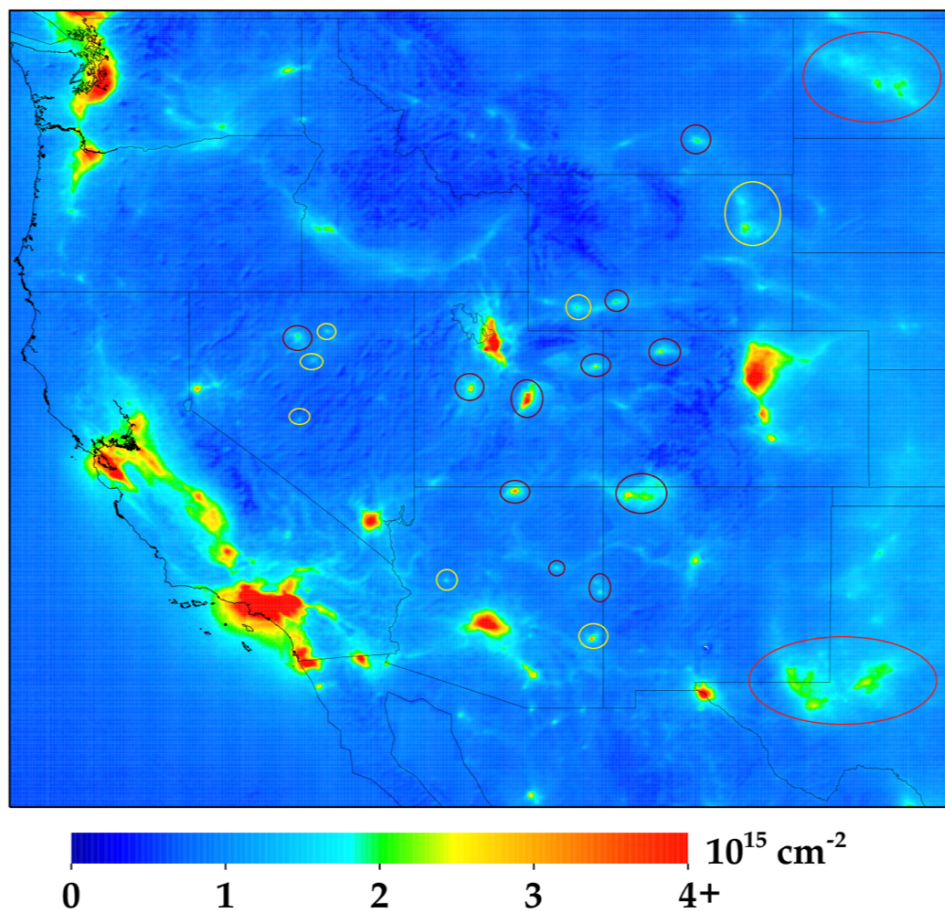
187 heterogeneities as the annual average, but with magnitude differences due to meteorology. It  
188 should be noted that September was specifically chosen for this analysis due to its propensity to  
189 have both less cloud coverage and snow cover than other months. If oversampling during winter  
190 months (i.e., Dec – March), which tend to have fewer ideal conditions for satellite retrievals of  
191 trace gases, oversampling times will need to be longer to achieve similar clarity.

192 When visually inspecting the CONUS TROPOMI NO<sub>2</sub> average during the initial twenty months  
193 of the TROPOMI record (May 1, 2018 – Dec 31, 2019) (Figure 2), we now start to see clear  
194 spatial heterogeneities across the domain. The largest U.S. cities can be seen and their  
195 magnitudes can be compared to each other (results further discussed later).



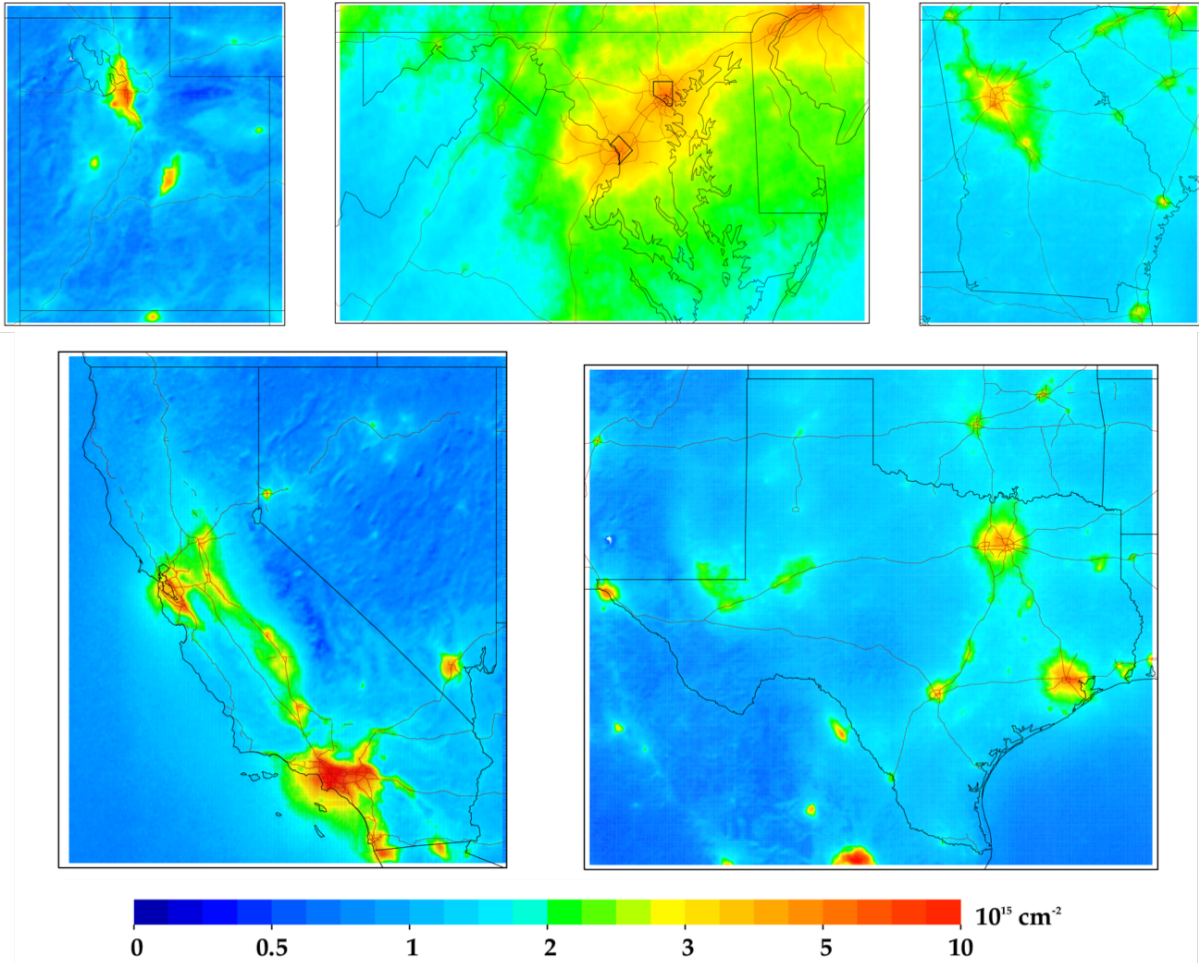
196  
197 **Figure 2.** TROPOMI NO<sub>2</sub> oversampled to 0.01° × 0.01° spatial resolution during May 1, 2018 –  
198 December 31, 2019. Only pixels exceeding a quality assurance flag of 0.75 are included.  
199 Equally important, smaller sources of NO<sub>2</sub> pollution can now be observed, and they are not  
200 spatially smeared into the background NO<sub>2</sub> concentration. For example, when magnifying the  
201 western United States (Figure 3), the roadway network and related activity in the Idaho Snake  
202 River valley can be clearly observed. Other examples are the copper mining operations in

203 eastern Arizona associated with the Morenci Mine, the coal mining operations in the Powder  
204 River Basin in eastern Wyoming, and to a lesser extent the gold mining operations associated  
205 with the Goldstrike mine in Nevada. In addition, NO<sub>2</sub> concentrations are clearly correlated with  
206 oil & gas operations in the Permian (Texas) and Bakken (North Dakota) basins (also discussed in  
207 (Dix et al., 2020)) and is > 5 times larger than the NO<sub>2</sub> in the rural areas upwind. Individual  
208 spikes in NO<sub>2</sub> associated with NO<sub>x</sub> emissions from large power plants (e.g., Navajo in Arizona,  
209 Craig in Colorado, Colstrip in Montana, North Valmy in Nevada, Four Corners/San Juan in New  
210 Mexico, Intermountain, Bonanza, Hunter/Huntington in Utah, Jim Bridger in Wyoming) can also  
211 be observed during this 2018-2019 period even though there have been large reductions (~85%)  
212 in the NO<sub>x</sub> emissions from most of these power plants since the introduction of the federally-  
213 mandated NO<sub>x</sub> SIP call in 2003.



214  
215 **Figure 3.** Same data shown in Figure 2, but now zoomed into the western United States. Power  
216 plants are outlined in dark magenta, mining operations in yellow, and oil & gas in bright red.

217 TROPOMI data is especially powerful in analyzing local variations in NO<sub>2</sub> pollution as  
218 compared to predecessor instruments. In Figure 4, we zoom into five different U.S. states, and in  
219 Table 1 we provide the largest NO<sub>2</sub> values in each state.



220

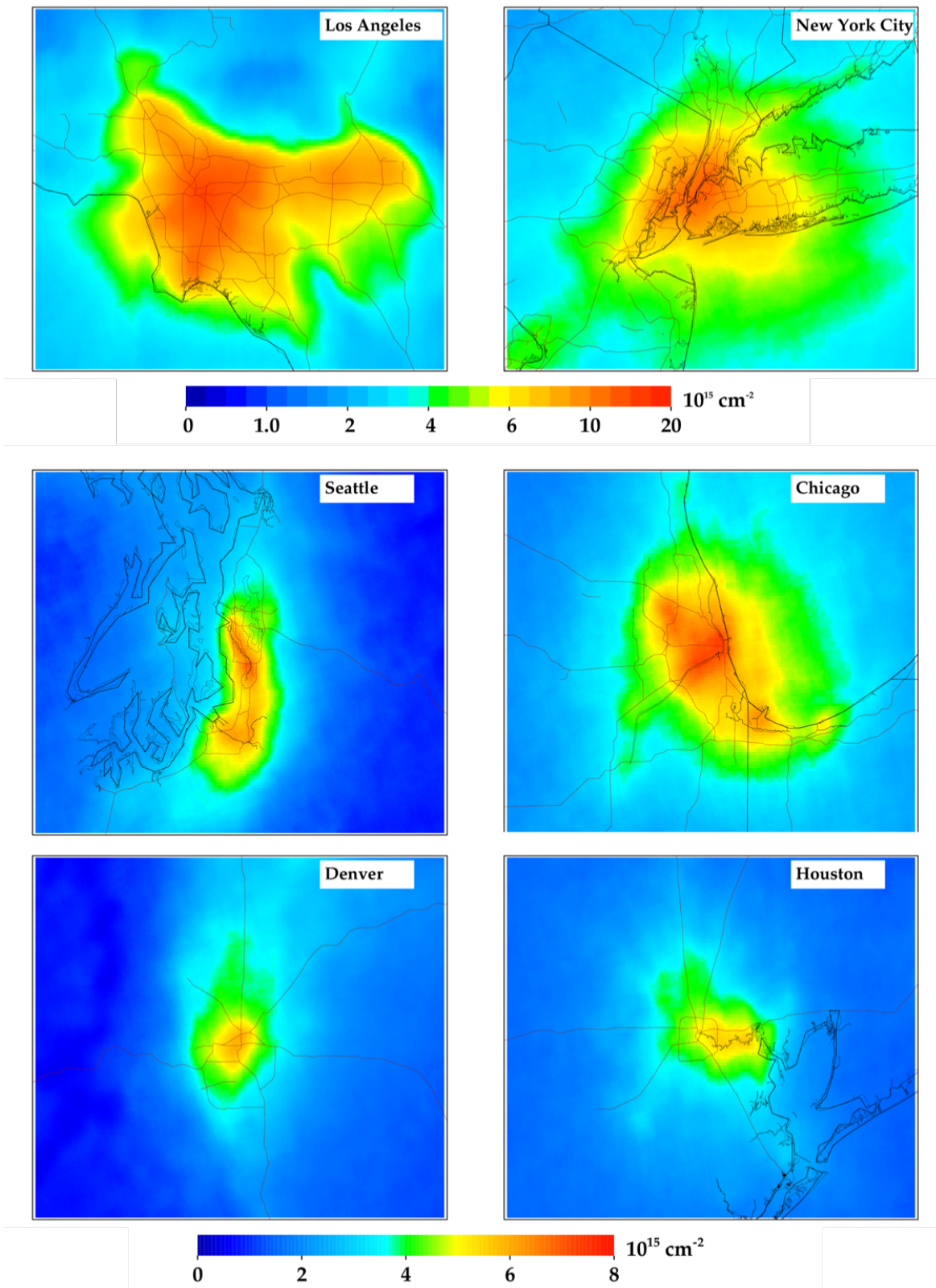
221 **Figure 4.** Same data shown in Figure 2, but now zoomed into 5 different U.S. states. Color bar  
222 has been adjusted to better differentiate spatial heterogeneities on a local scale.

223

224 **Table 1.** Largest NO<sub>2</sub> column value in each U.S. state during the May 1, 2018 – Dec 31, 2018  
 225 period. Ordered by largest to smallest maximum value.

State	Lat	Lon	Value	Detailed location
CA	34.03	-118.18	1.41E+16	E Los Angeles, CA
NY	40.72	-73.97	1.13E+16	East River, Brooklyn, NY
NJ	40.69	-74.14	9.75E+15	Port Newark, NJ
IL	41.82	-87.77	7.31E+15	Cicero, Chicago, IL (near MDW)
WA	47.46	-122.26	6.90E+15	Tukwila, WA (SE Seattle)
IN	41.66	-87.47	6.28E+15	E Chicago, IN (Steel Mill)
UT	40.71	-111.9	6.18E+15	S Salt Lake City, UT
CO	39.76	-105.02	5.98E+15	Highland, Denver, CO
PA	39.95	-75.16	5.95E+15	Downtown Philadelphia, PA
AZ	33.47	-112.15	5.87E+15	Cuatro Palmas, Phoenix, AZ
MI	42.31	-83.11	5.74E+15	Detroit, MI
TX	29.74	-95.14	5.58E+15	Deer Park, Houston, TX
CT	41	-73.67	5.46E+15	Greenwich, CT
NV	36.1	-115.18	4.97E+15	Las Vegas Strip, Las Vegas, NV
MD	39.28	-76.6	4.94E+15	Port of Baltimore, Baltimore, MD
DC	38.89	-77.01	4.65E+15	Capitol Hill, Washington, DC
GA	33.64	-84.42	4.65E+15	Hartsfield Airport, Atlanta, GA
VA	38.88	-77.05	4.59E+15	Pentagon, Arlington, VA
DE	39.8	-75.37	4.34E+15	Claymont, Wilmington, DE
OR	45.52	-122.65	4.25E+15	Buckman, Portland, OR
KY	38.18	-85.73	4.21E+15	Louisville, KY (Airport)
OH	39.12	-84.54	4.20E+15	Cincinnati, OH
MA	42.37	-71.06	4.14E+15	Charlestown, Boston, MA (near BOS)
LA	29.93	-90.14	3.98E+15	Mississippi River, New Orleans, LA
NC	35.24	-80.85	3.76E+15	Catawba, NC (near Marshall Steam SPP)
WV	38.94	-82.11	3.68E+15	Lakin, WV (near Gavin PP)
MO	38.68	-90.19	3.67E+15	Mississippi River, St Louis, MO
KS	39.12	-94.6	3.61E+15	Missouri River, Kansas City, KS
TN	36.16	-86.77	3.52E+15	Nashville, TN
FL	25.85	-80.34	3.40E+15	Medley, Miami, FL
WI	42.86	-87.82	3.40E+15	Oak Creek, WI (near Oak Creek PP)
MN	44.97	-93.24	3.28E+15	Mississippi River, Minneapolis, MN
AL	33.52	-86.82	3.21E+15	Fountain Heights, Birmingham, AL
RI	41.8	-71.41	2.88E+15	S Providence, RI
IA	41.25	-95.88	2.79E+15	Council Bluffs, IA
NE	41.25	-95.88	2.79E+15	Missouri River, Omaha, NE
OK	36.16	-96	2.64E+15	Tulsa, OK
WY	43.69	-105.32	2.52E+15	Thunder Basin Coal, WY
SC	32.88	-79.99	2.52E+15	N Charleston, SC
NM	35.11	-106.62	2.51E+15	Albuquerque, NM
AR	35.12	-90.1	2.46E+15	W Memphis, AR
ID	43.58	-116.23	2.30E+15	Boise, ID (Airport)
ND	47.35	-101.81	2.24E+15	Beulah, ND (near Dakota Gasification Co)
MT	45.86	-106.57	2.20E+15	Colstrip, MT (near Colstrip PP)
NH	42.94	-70.81	1.93E+15	Hampton, NH
ME	43.66	-70.29	1.90E+15	Portland, ME
MS	32.34	-90.19	1.77E+15	Jackson, MS
SD	43.6	-96.74	1.53E+15	N Sioux Falls, SD
VT	42.91	-73.18	1.49E+15	Wilmington, VT

227 In Figure 5, we zoom into six different U.S. cities. In each instance, the oversampled TROPOMI  
228 NO<sub>2</sub> images exhibit features that match known NO<sub>x</sub> emissions patterns. The larger NO<sub>2</sub> values  
229 correlate very well to the interstate network, population density, and industrial activity hubs  
230 (such as manufacturing facilities, airports, and shipping ports). For example, in the image of  
231 Maryland, the largest value is observed at the Baltimore Harbor, which is a confluence of several  
232 major highways, a large shipping port, the city incinerator, and many industrial facilities.  
233 Similarly, the largest values in Chicago exist along the I-55 corridor which has a high traffic  
234 volume and a high-density of industrial facilities, with secondary maxima at the O'Hare  
235 International airport and the U.S. Steel mill in East Chicago, Indiana. In Los Angeles, the spatial  
236 pattern matches the basin outline very well, with the largest values between downtown Los  
237 Angeles and Long Beach. In Houston, Texas the largest values are nearest to the petrochemical  
238 refining facilities east of town. For all cases, TROPOMI can accurately quantify the relative  
239 relationship between the largest sources of NO<sub>x</sub> emissions and NO<sub>2</sub> concentrations.

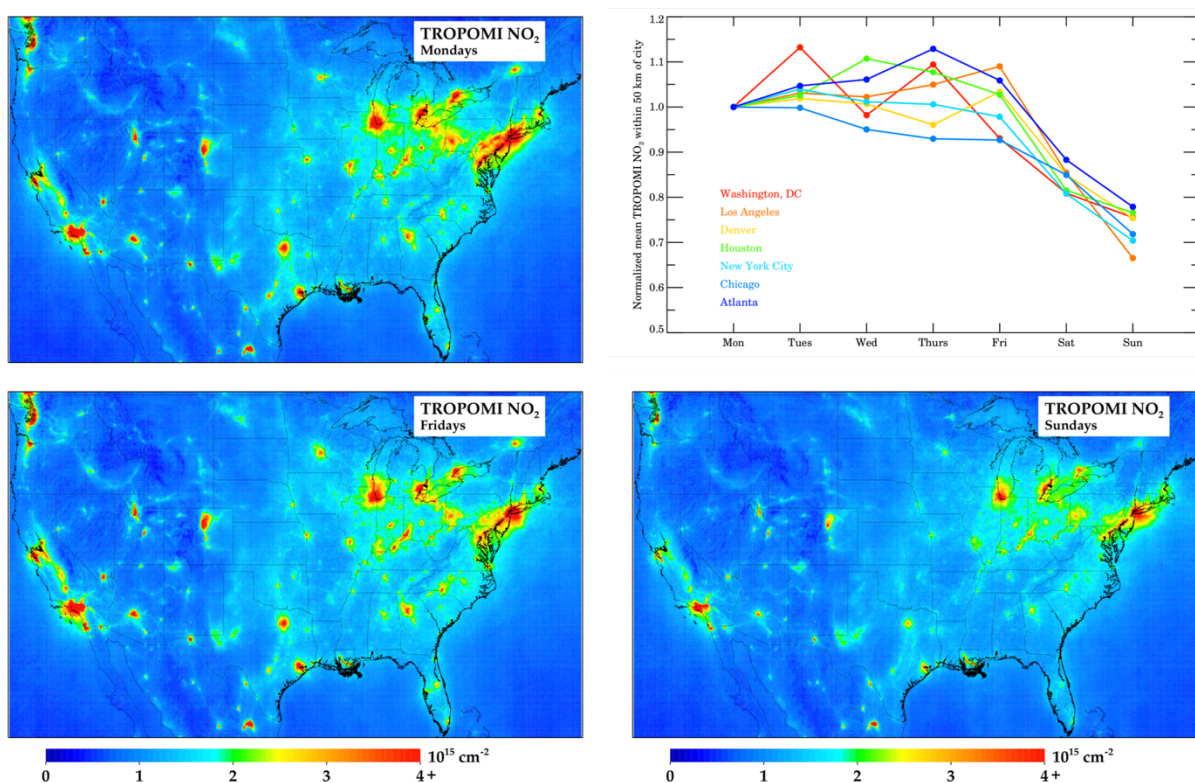


240

241 **Figure 5.** Same data shown in Figure 2, but now zoomed into 6 different U.S. cities. Color bar  
 242 has been adjusted to better differentiate spatial heterogeneities on a local scale.

243 **Day-of-the-week relationships**

244 A common use of oversampled satellite data is in investigating the weekly cycle of NO<sub>x</sub>  
245 emissions. In Figure 6, we show the weekly pattern of NO<sub>2</sub> across CONUS for three different  
246 days of the week as well as the full weekly cycle in seven U.S. cities. In all cities, the NO<sub>2</sub>  
247 appears to be approximately equivalent amongst all weekdays with some minor exceptions. NO<sub>2</sub>  
248 pollution is 2.5% larger on Tuesday than a typical weekday, while Mondays and Fridays have  
249 1.4% and 1.3% lower NO<sub>2</sub> pollution than a typical weekday. On Saturdays, NO<sub>2</sub> is 16% lower  
250 than the weekday averages, and on Sundays 24% lower.



251 **Figure 6.** Weekly variations in column NO<sub>2</sub>. (Top left) TROPOMI NO<sub>2</sub> during Mondays.  
252 (Bottom left) TROPOMI NO<sub>2</sub> during Fridays. (Top right) Weekly variation of TROPOMI NO<sub>2</sub>  
253 in 7 U.S. cities normalized to Mondays. (Bottom right) TROPOMI NO<sub>2</sub> during Sundays.

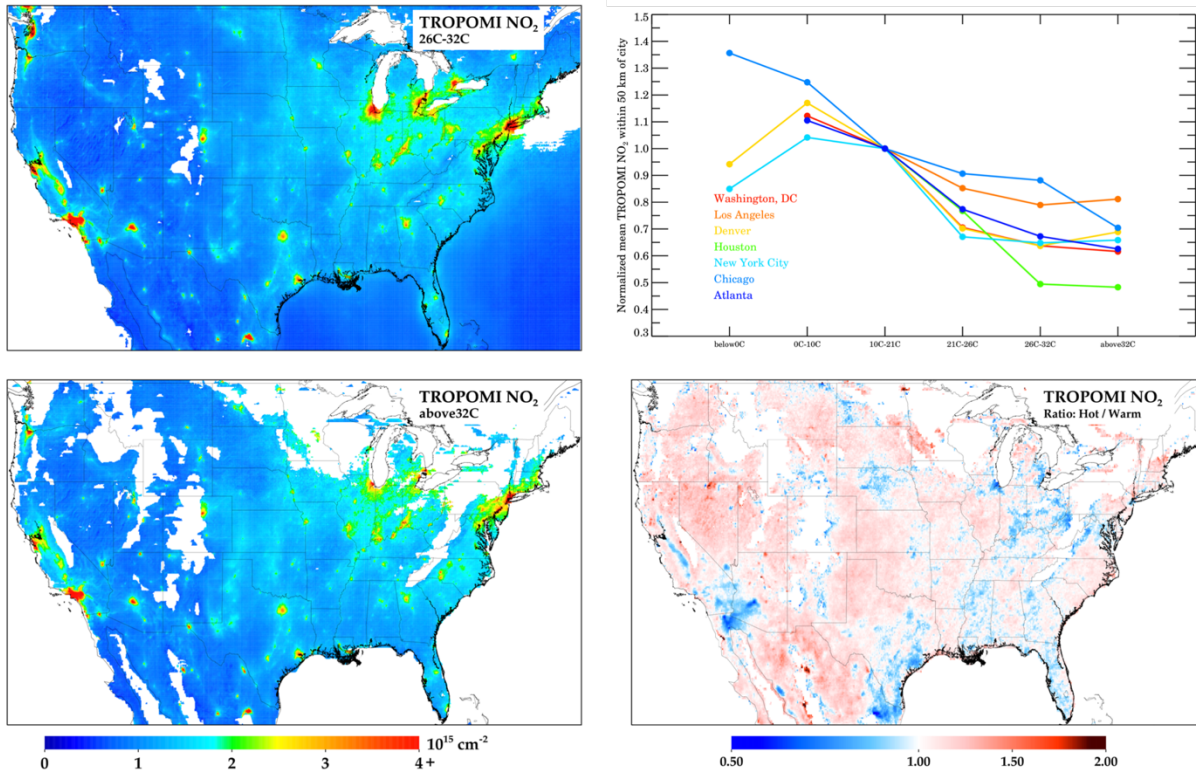
254 It is interesting to see the differences in the weekday patterns amongst the cities. In Chicago and  
255 Washington, D.C., column NO<sub>2</sub> is 10% lower on Fridays compared to earlier days in the week.  
256 Conversely, in Los Angeles and Denver, NO<sub>2</sub> is larger on Fridays as compared to previous days  
257 of the week. In Chicago and Washington D.C., we hypothesize that this may be an indication of  
258 teleworking on Fridays. Conversely, the cities with higher pollution on Fridays, are generally  
259

260 located in mountain valleys with stagnant winds – the valleys may be facilitating an  
261 accumulation of pollution during the week.

262 When analyzing the weekday/weekend differences, there should be some consideration for the  
263 difference in traffic patterns and general activity between weekends and weekdays. On  
264 weekends, traffic counts generally peak in the early afternoon, while on weekdays traffic counts  
265 peak in the evening, with a secondary peak in the early morning (de Foy, 2018). Since the  
266 satellite observation is acquired in the early afternoon, we suggest that the 24-hour averaged  
267  $\text{NO}_x$  emissions difference between weekdays and weekends may be even greater than implied by  
268 the satellite data. The soon-to-be-launched TEMPO instrument, a geostationary satellite, will  
269 hopefully be able to better quantify the morning and evening differences of  $\text{NO}_x$  emissions  
270 (Chance et al., 2019; Penn & Holloway, 2020; Zoogman et al., 2017).

#### 271 **Hot vs. Warm Days**

272 In Figure 7, we show the variation in column  $\text{NO}_2$  as a function of the daily maximum 2-meter  
273 temperature (T2m-Max). Due to varying climates across the U.S. most cities do not have values  
274 for all temperature bins. In general, as temperatures increase,  $\text{NO}_2$  decreases; this is primarily  
275 driven by  $j(\text{NO}_2)$  which increases with stronger sunlight. When temperatures are  $>32^\circ\text{C}$ , we  
276 observe a leveling with increasing temperature. This may be related to increasing anthropogenic  
277  $\text{NO}_x$  emissions (Abel et al., 2017; He et al., 2013) at high temperatures despite a shorter  $\text{NO}_2$   
278 lifetime. This may also be driven by biogenic or natural causes, such as the faster dissociation of  
279 peroxy-acyl nitrates (PANs) or increased soil  $\text{NO}_x$  emissions (Rasool et al., 2019; Romer et al.,  
280 2018) at hot temperatures. The latter reasons are likely causing rural areas to observe increases  
281 in  $\text{NO}_2$  as temperatures warm above  $32^\circ\text{C}$ . The temperature-driven stabilization of  $\text{NO}_2$  at very  
282 high temperatures appears to hold for all cities except Chicago.



283

284 **Figure 7.** Temperature variations in column NO<sub>2</sub>. (Top left) TROPOMI NO<sub>2</sub> when maximum  
 285 daily 2-m temperature (T2m-Max) is between 26°C – 32°C (Warm; 80°F – 90°F); only areas  
 286 were >10 valid pixels are shown. (Bottom left) TROPOMI NO<sub>2</sub> when T2m-Max is greater than  
 287 32°C (Hot; 90°F); only areas were >10 valid pixels are shown. (Top right) Temperature variation  
 288 of TROPOMI NO<sub>2</sub> in 7 U.S. cities normalized to 10°C – 21°C (50°F – 70°F). (Bottom right)  
 289 Ratio between bottom left and bottom right panel.

290

### 291 Relationship with PM<sub>2.5</sub>

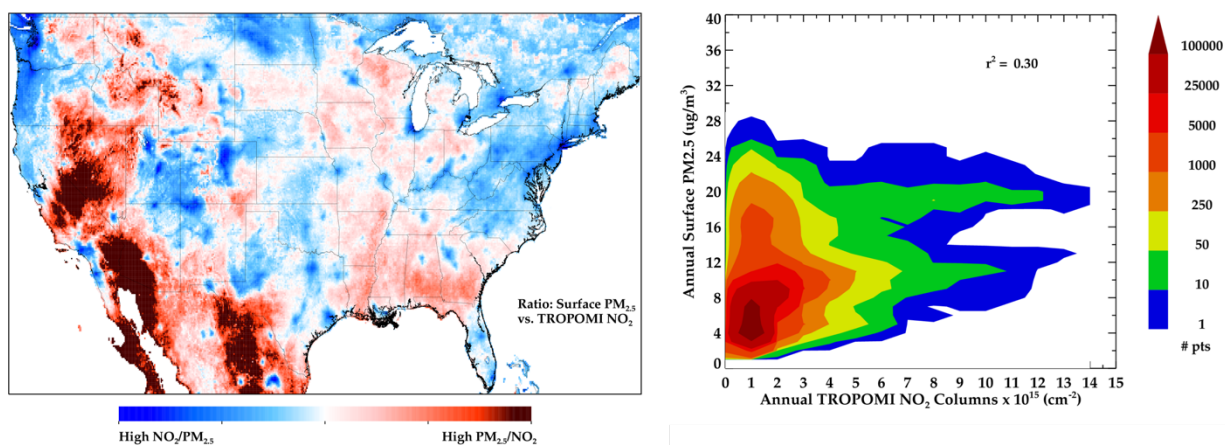
292 To understand the spatial pattern of NO<sub>2</sub> in comparison to PM<sub>2.5</sub>, we compare TROPOMI annual  
 293 averages of column NO<sub>2</sub> to estimates of surface-level PM<sub>2.5</sub> (VanDonkelaar et al., 2019). Both  
 294 pollutants have generally short atmospheric lifetimes and often have similar regional patterns. In  
 295 Figure 8, we depict the ratio between normalized TROPOMI NO<sub>2</sub> and normalized surface PM<sub>2.5</sub>  
 296 using the equation below.

297

$$\frac{PM_{2.5}/\overline{PM_{2.5}}}{NO_2/\overline{NO_2}}$$

298 The red color in Figure 8 indicates that PM<sub>2.5</sub> is relatively larger than NO<sub>2</sub> and blue indicates that  
 299 NO<sub>2</sub> is relatively larger than PM<sub>2.5</sub>. There are instances, especially in cities, where PM<sub>2.5</sub> and

300 NO<sub>2</sub> are both greater than the CONUS mean, but that one pollutant is much larger than the mean  
301 and the other value is only slightly larger than the mean.



302  
303 **Figure 8.** (Left) Ratio of oversampled 2019 TROPOMI NO<sub>2</sub> / 2016 Surface PM<sub>2.5</sub>. (Right)  
304 Scatterplot of the two datasets. 2016 is latest year of the 0.01° × 0.01° PM<sub>2.5</sub> dataset (van  
305 Donkelaar et al., 2019) and is used for illustrative purposes. Spatial heterogeneities of annual  
306 PM<sub>2.5</sub> is likely similar between 2016 and 2019.

307 In major cities (e.g., New York City, Chicago, Los Angeles), NO<sub>2</sub> is more elevated from the  
308 mean CONUS concentration compared to PM<sub>2.5</sub>. This is also true regionally in the Northeast and  
309 Pacific Northwest. Conversely, PM<sub>2.5</sub> is relatively elevated compared to the mean in four  
310 distinct rural CONUS regions: the desert Southwest, the Intermountain West, the Central Plains,  
311 and the Southeast. In the Southwest this is driven by dust. In the Intermountain West, this is  
312 likely driven by wildfires. In the Southeast and Central Plains, it is most likely driven by a  
313 combination of biogenic aerosols (e.g., secondary organic aerosols) and agricultural operations.

314 We then compare the NO<sub>2</sub> and PM<sub>2.5</sub> datasets using a scatterplot. We find low correlation  
315 between column NO<sub>2</sub> and surface PM<sub>2.5</sub> ( $r^2 = 0.30$ ). At high TROPOMI NO<sub>2</sub> values, PM<sub>2.5</sub> is  
316 moderately elevated, but at low TROPOMI NO<sub>2</sub> values, there is a range of distribution of PM<sub>2.5</sub>  
317 with no correlation. This is in general agreement with studies showing that NO<sub>2</sub> hotspots are  
318 dominated by local and regional components, while PM<sub>2.5</sub> is dominated by regional and long-  
319 range components, with a lesser influence of local sources (Wang et al., 2020). Nevertheless, we  
320 find it important to demonstrate that TROPOMI NO<sub>2</sub> does not appear to be helpful in predicting  
321 surface PM<sub>2.5</sub> in the US.

## 322 **Conclusions**

323 This study investigates the capabilities of the Tropospheric Monitoring Instrument (TROPOMI)  
324 in observing the spatial and temporal patterns of NO<sub>2</sub> pollution in the Continental United States  
325 (CONUS). Here, we demonstrate that TROPOMI can capture fine-scale spatial heterogeneities  
326 in urban areas, such as hotspots related to airport/shipping operations and high traffic areas; this  
327 type of spatial precision cannot be matched by predecessor satellite instruments over short  
328 timescales (<1 year). We find that Saturday and Sunday concentrations are 16% and 24% lower  
329 respectively than during weekdays, with the caveat that diurnal emissions patterns vary among  
330 weekdays and weekends. We also analyze the effects of hot temperatures (>32°C) on NO<sub>2</sub>  
331 column amounts and find that column NO<sub>2</sub> is generally larger on the hottest days as compared to  
332 warm days (26°C - 32°C). Finally, we compare column NO<sub>2</sub> with estimates of surface PM<sub>2.5</sub> and  
333 find fairly poor correlation, suggesting that NO<sub>2</sub> and PM<sub>2.5</sub> are not well correlated in CONUS.

334 For this work, we rely on the operational TROPOMI NO<sub>2</sub> algorithm, which underestimates  
335 tropospheric vertical column NO<sub>2</sub> in urban areas. Previous studies suggest that this underestimate  
336 is due to the air mass factor (AMF) and ~5km pixel size which cannot resolve street-level  
337 variations in concentrations (Goldberg, Lu, Streets, et al., 2019; Griffin et al., 2019; Judd et al.,  
338 2019, 2020; Zhao et al., 2020); investigating the effects of the AMF bias on trends as well as  
339 investigating the effects of the pixels sizes will be the subject of future work. Also, there may be  
340 a clear-sky bias (Geddes et al., 2012) associated with any satellite retrieval, but the general  
341 spatial heterogeneities of NO<sub>2</sub> pollution, should be similar amongst all types of weather  
342 conditions, when averaged over long timeframes. Lastly, interpreting results from polar-orbiting  
343 satellite instruments such as TROPOMI, should be made with some caution due to the mid-day  
344 only data collection time. Work quantifying this bias has shown that NO<sub>2</sub> column measurements  
345 are lower and incrementally more spatially homogeneous in the afternoon than during the  
346 morning (Chong et al., 2018; Fishman et al., 2008; Herman et al., 2019; Knepp et al., 2015; Penn  
347 & Holloway, 2020; Tzortziou et al., 2015); it is likely that data from geostationary platforms  
348 such as TEMPO (Zoogman et al., 2017), GEMS (W. J. Choi, 2018), and Sentinel 4  
349 (Timmermans et al., 2019), will be able to provide further insight on this time-of-day bias.

350 Because TROPOMI can observe and measure NO<sub>2</sub> increases attributed to relatively small  
351 sources, future work should be able to quantify emissions from small sources (e.g., industrial

352 activities, small wildfires) that had previously gone undetected from predecessor space-based  
353 instruments. Furthermore, due to the instrument's excellent stability, precision, and spatial  
354 resolution, it is no longer necessary to average over 6+ months of data to gain a clear depiction  
355 of regional NO<sub>2</sub> abundances; instead monthly, weekly or even daily aggregations could suffice  
356 for many purposes. The examples presented here demonstrate how TROPOMI NO<sub>2</sub> satellite data  
357 can be advantageous for policymakers requesting information at high spatial resolution and short  
358 timescales, in order to assess, devise, and evaluate regulations. Future health impact assessment  
359 studies can use the high-spatial resolution capabilities of TROPOMI NO<sub>2</sub> to investigate  
360 disparities in traffic-related air pollution exposure and associated health effects between  
361 neighborhoods and population sub-groups within cities.

362 **Acknowledgments**

363 This work has been supported by the Department of Energy, Office of Fossil Energy. This work  
364 has also been sponsored by a Health and Air Quality (HAQ) grant (award #: 80NSSC19K0193),  
365 and two Atmospheric Composition Modeling and Analysis Program grants. We would also like  
366 to acknowledge valuable comments during the manuscript preparation from Joel Dreessen of  
367 Maryland Department of the Environment. TROPOMI NO<sub>2</sub> data can be freely downloaded from  
368 the European Space Agency Copernicus Open Access Hub or the NASA EarthData Portal  
369 (<http://doi.org/10.5270/S5P-s4ljg54>). ERA5 can be freely downloaded from the Copernicus  
370 Climate Change (C3S) climate data store (CDS)  
371 (<https://cds.climate.copernicus.eu/#!/search?text=ERA5&type=dataset>). The submitted  
372 manuscript has been created by UChicago Argonne, LLC, Operator of Argonne National  
373 Laboratory (“Argonne”). Argonne, a US Department of Energy Office of Science laboratory, is  
374 operated under contract no. DE-AC02-06CH11357.

375

376 **References**

- 377 Abel, D. W., Holloway, T., Kladar, R. M., Meier, P., Ahl, D., Harkey, M., & Patz, J. (2017).  
378 Response of Power Plant Emissions to Ambient Temperature in the Eastern United States.  
379 *Environmental Science and Technology*, 51(10), 5838–5846.  
380 <https://doi.org/10.1021/acs.est.6b06201>
- 381 Achakulwisut, P., Brauer, M., Hystad, P., & Anenberg, S. C. (2019). Global, national, and urban  
382 burdens of paediatric asthma incidence attributable to ambient NO<sub>2</sub> pollution: estimates  
383 from global datasets. *Lancet Planet Health*. [https://doi.org/10.1016/S2542-5196\(19\)30046-4](https://doi.org/10.1016/S2542-5196(19)30046-4)
- 384 Anenberg, S. C., Henze, D. K., Tinney, V., Kinney, P. L., Raich, W., Fann, N., et al. (2018).  
385 Estimates of the Global Burden of Ambient PM<sub>2.5</sub>, Ozone, and NO<sub>2</sub> on Asthma Incidence  
386 and Emergency Room Visits. *Environmental Health Perspectives*, 126(10), 107004.  
387 <https://doi.org/10.1289/EHP3766>
- 388 Beirle, S., Platt, U., Wenig, M., & Wagner, T. (2003). Weekly cycle of NO<sub>2</sub> by GOME  
389 measurements: A signature of anthropogenic sources. *Atmospheric Chemistry and Physics*,  
390 3(6), 2225–2232. <https://doi.org/10.5194/acp-3-2225-2003>
- 391 Beirle, S., Boersma, K. F., Platt, U., Lawrence, M. G., & Wagner, T. (2011). Megacity  
392 Emissions and Lifetimes of Nitrogen Oxides Probed from Space. *Science*, 333(6050), 1737–  
393 1739. <https://doi.org/10.1126/science.1207824>
- 394 Beirle, S., Borger, C., Dörner, S., Li, A., Hu, Z., Liu, F., et al. (2019). Pinpointing nitrogen oxide  
395 emissions from space. *Science Advances*, 5(11), eaax9800.  
396 <https://doi.org/10.1126/sciadv.aax9800>
- 397 Bell, M. L. (2004). Ozone and Short-term Mortality in 95 US Urban Communities, 1987-2000.  
398 *Jama*, 292(19), 2372. <https://doi.org/10.1001/jama.292.19.2372>
- 399 Bell, M. L., Peng, R. D., & Dominici, F. (2006). The exposure-response curve for ozone and risk  
400 of mortality and the adequacy of current ozone regulations. *Environmental Health*  
401 *Perspectives*, 114(4), 532–536. <https://doi.org/10.1289/ehp.8816>
- 402 Boersma, K. F., Eskes, H. J., Richter, A., De Smedt, I., Lorente, A., Beirle, S., et al. (2018).  
403 Improving algorithms and uncertainty estimates for satellite NO<sub>2</sub> retrievals: results from the  
404 quality assurance for the essential climate variables (QA4ECV) project. *Atmospheric*  
405 *Measurement Techniques*, 11(12), 6651–6678. <https://doi.org/10.5194/amt-11-6651-2018>
- 406 Bovensmann, H., Burrows, J. P., Buchwitz, M., Frerick, J., Noël, S., Rozanov, V. V., et al.  
407 (1999). SCIAMACHY: Mission Objectives and Measurement Modes. *Journal of the*  
408 *Atmospheric Sciences*, 56(2), 127–150. [https://doi.org/10.1175/1520-0469\(1999\)056<0127:SMOAMM>2.0.CO;2](https://doi.org/10.1175/1520-0469(1999)056<0127:SMOAMM>2.0.CO;2)
- 410 Broeckaert, F., Arsalane, K., Hermans, C., Bergamaschi, E., Brustolin, A., Mutti, A., & Bernard,  
411 A. (1999). Lung epithelial damage at low concentrations of ambient ozone. *Lancet*,  
412 353(9156), 900–901. [https://doi.org/10.1016/S0140-6736\(99\)00540-1](https://doi.org/10.1016/S0140-6736(99)00540-1)
- 413 Burnett, R. T., Stieb, D., Brook, J. R., Cakmak, S., Dales, R., Raizenne, M., et al. (2004).  
414 Associations between short-term changes in nitrogen dioxide and mortality in Canadian

- 415 cities. *Archives of Environmental Health*, 59(5), 228–236.  
416 <https://doi.org/10.3200/AEOH.59.5.228-236>
- 417 Burns, D. A., Gay, D. A., & Lehmann, C. M. B. (2016). Acid rain and its environmental effects:  
418 Recent scientific advances. *Atmospheric Environment*, 146, 1–4.  
419 <https://doi.org/10.1016/J.ATMOSENV.2016.10.019>
- 420 Burrows, J. P., Weber, M., Buchwitz, M., Rozanov, V., Ladstatter-Weibenmayer, A., Richter,  
421 A., et al. (1999). The Global Ozone Monitoring Experiment (GOME): Mission Concept and  
422 First Scientific Results. *Journal of Atmospheric Sciences*, 56, 151–175.  
423 [https://doi.org/10.1175/1520-0469\(1999\)056<0151:TGOMEG>2.0.CO;2](https://doi.org/10.1175/1520-0469(1999)056<0151:TGOMEG>2.0.CO;2)
- 424 Canty, T. P., Hemberck, L., Vinciguerra, T. P., Anderson, D. C., Goldberg, D. L., Carpenter, S.  
425 F., et al. (2015). Ozone and NO<sub>x</sub> chemistry in the eastern US: Evaluation of  
426 CMAQ/CB05 with satellite (OMI) data. *Atmospheric Chemistry and Physics*, 15(19),  
427 10965–10982. <https://doi.org/10.5194/acp-15-10965-2015>
- 428 Castellanos, P., & Boersma, K. F. (2012). Reductions in nitrogen oxides over Europe driven by  
429 environmental policy and economic recession. *Scientific Reports*, 2(2), 1–7.  
430 <https://doi.org/10.1038/srep00265>
- 431 Chance, K., Liu, X., Miller, C. C., González Abad, G., Huang, G., Nowlan, C., et al. (2019).  
432 TEMPO Green Paper: Chemistry, physics, and meteorology experiments with the  
433 Tropospheric Emissions: monitoring of pollution instrument. In S. P. Neeck, T. Kimura, &  
434 P. Martimort (Eds.), *Sensors, Systems, and Next-Generation Satellites XXIII* (Vol. 11151, p.  
435 10). SPIE. <https://doi.org/10.1117/12.2534883>
- 436 Choi, S., Lamsal, L. N., Follette-Cook, M., Joiner, J., Krotkov, N. A., Swartz, W. H., et al.  
437 (2019). Assessment of NO<sub>2</sub> observations during DISCOVER-AQ and KORUS-AQ field  
438 campaigns. *AMTD*. <https://doi.org/10.5194/amt-2019-338>
- 439 Choi, W. J. (2018). Introducing the geostationary environment monitoring spectrometer. *Journal*  
440 *of Applied Remote Sensing*, 12(04), 1. <https://doi.org/10.1117/1.JRS.12.044005>
- 441 Chong, H., Lee, H., Koo, J. H., Kim, J., Jeong, U., Kim, W., et al. (2018). Regional  
442 characteristics of NO<sub>2</sub> column densities from pandora observations during the MAPS-Seoul  
443 campaign. *Aerosol and Air Quality Research*, 18(9), 2207–2219.  
444 <https://doi.org/10.4209/aaqr.2017.09.0341>
- 445 Cohen, A. J., Brauer, M., Burnett, R. T., Anderson, H. R., Frostad, J., Estep, K., et al. (2017).  
446 Estimates and 25-year trends of the global burden of disease attributable to ambient air  
447 pollution: an analysis of data from the Global Burden of Diseases Study 2015. *The Lancet*,  
448 389(10082), 1907–1918. [https://doi.org/10.1016/S0140-6736\(17\)30505-6](https://doi.org/10.1016/S0140-6736(17)30505-6)
- 449 Cooper, M. J., Martin, R. V., Padmanabhan, A., & Henze, D. K. (2017). Comparing mass  
450 balance and adjoint methods for inverse modeling of nitrogen dioxide columns for global  
451 nitrogen oxide emissions. *Journal of Geophysical Research*, 122(8), 4718–4734.  
452 <https://doi.org/10.1002/2016JD025985>
- 453 Dix, B., Bruin, J., Roosenbrand, E., Vlemmix, T., Francoeur, C., Gorchov-Negron, A., et al.  
454 (2020). Nitrogen Oxide Emissions from U.S. Oil and Gas Production: Recent Trends and

- 455 Source Attribution. *Geophysical Research Letters*, 47(1), 2019GL085866.  
456 <https://doi.org/10.1029/2019GL085866>
- 457 Duncan, B. N., Lamsal, L. N., Thompson, A. M., Yoshida, Y., Lu, Z., Streets, D. G., et al.  
458 (2016). A space-based, high-resolution view of notable changes in urban NO<sub>x</sub> pollution  
459 around the world (2005-2014). *Journal of Geophysical Research: Atmospheres*, 121(2),  
460 976–996. <https://doi.org/10.1002/2015JD024121>
- 461 Fishman, J., Bowman, K. W., Burrows, J. P., Richter, A., Chance, K. V., Edwards, D. P., et al.  
462 (2008). Remote Sensing of Tropospheric Pollution from Space. *Bulletin of the American*  
463 *Meteorological Society*, 89(6), 805–822. <https://doi.org/10.1175/2008BAMS2526.1>
- 464 de Foy, B. (2018). City-level variations in NO<sub>x</sub> emissions derived from hourly monitoring data  
465 in Chicago. *Atmospheric Environment*, 176(x), 128–139.  
466 <https://doi.org/10.1016/j.atmosenv.2017.12.028>
- 467 de Foy, B., Wilkins, J. L., Lu, Z., Streets, D. G., & Duncan, B. N. (2014). Model evaluation of  
468 methods for estimating surface emissions and chemical lifetimes from satellite data.  
469 *Atmospheric Environment*, 98, 66–77. <https://doi.org/10.1016/j.atmosenv.2014.08.051>
- 470 de Foy, B., Lu, Z., Streets, D. G., Lamsal, L. N., & Duncan, B. N. (2015). Estimates of power  
471 plant NO<sub>x</sub> emissions and lifetimes from OMI NO<sub>2</sub> satellite retrievals. *Atmospheric*  
472 *Environment*, 116(2), 1–11. <https://doi.org/10.1016/j.atmosenv.2015.05.056>
- 473 Geddes, J. A., Murphy, J. G., O'Brien, J. M., & Celarier, E. A. (2012). Biases in long-term NO<sub>2</sub>  
474 averages inferred from satellite observations due to cloud selection criteria. *Remote Sensing*  
475 *of Environment*, 124(2), 210–216. <https://doi.org/10.1016/j.rse.2012.05.008>
- 476 Geddes, J. A., Martin, R. V., Boys, B. L., & van Donkelaar, A. (2016). Long-Term Trends  
477 Worldwide in Ambient NO<sub>2</sub> Concentrations Inferred from Satellite Observations.  
478 *Environmental Health Perspectives*, 124(3), 281–289. <https://doi.org/10.1289/ehp.1409567>
- 479 van Geffen, J., Boersma, K. F., Eskes, H., Sneep, M., ter Linden, M., Zara, M., & Veeffkind, J. P.  
480 (2020). S5P TROPOMI NO<sub>2</sub> slant column  
481 retrieval: method, stability, uncertainties and comparisons with OMI. *Atmospheric*  
482 *Measurement Techniques*, 13(3), 1315–1335. <https://doi.org/10.5194/amt-13-1315-2020>
- 483 Georgoulias, A. K., van der A, R. J., Stammes, P., Boersma, K. F., & Eskes, H. J. (2019). Trends  
484 and trend reversal detection in 2 decades of tropospheric NO<sub>2</sub> satellite observations.  
485 *Atmospheric Chemistry and Physics*, 19(9), 6269–6294. [https://doi.org/10.5194/acp-19-](https://doi.org/10.5194/acp-19-6269-2019)  
486 [6269-2019](https://doi.org/10.5194/acp-19-6269-2019)
- 487 Goldberg, D. L., Lamsal, L. N., Loughner, C. P., Swartz, W. H., Lu, Z., & Streets, D. G. (2017).  
488 A high-resolution and observationally constrained OMI NO<sub>2</sub> satellite retrieval. *Atmospheric*  
489 *Chemistry and Physics*, 17(18), 11403–11421. <https://doi.org/10.5194/acp-17-11403-2017>
- 490 Goldberg, D. L., Saide, P. E., Lamsal, L. N., de Foy, B., Lu, Z., Woo, J.-H., et al. (2019). A top-  
491 down assessment using OMI NO<sub>2</sub> suggests an underestimate in the NO<sub>x</sub> emissions  
492 inventory in Seoul, South Korea, during KORUS-AQ. *Atmospheric Chemistry and Physics*,  
493 19(3), 1801–1818. <https://doi.org/10.5194/acp-19-1801-2019>
- 494 Goldberg, D. L., Lu, Z., Streets, D. G., de Foy, B., Griffin, D., McLinden, C. A., et al. (2019).

495 Enhanced Capabilities of TROPOMI NO<sub>2</sub> : Estimating NO<sub>x</sub> from North American Cities  
496 and Power Plants. *Environmental Science & Technology*, acs.est.9b04488.  
497 <https://doi.org/10.1021/acs.est.9b04488>

498 Goldberg, D. L., Lu, Z., Oda, T., Lamsal, L. N., Liu, F., Griffin, D., et al. (2019). Exploiting  
499 OMI NO<sub>2</sub> satellite observations to infer fossil-fuel CO<sub>2</sub> emissions from U.S. megacities.  
500 *Science of The Total Environment*, 695, 133805.  
501 <https://doi.org/10.1016/j.scitotenv.2019.133805>

502 de Gouw, J. A., Veefkind, J. P., Roosenbrand, E., Dix, B., Lin, J. C., Landgraf, J., & Levelt, P. F.  
503 (2020). Daily Satellite Observations of Methane from Oil and Gas Production Regions in  
504 the United States. *Scientific Reports*, 10(1), 1379. [https://doi.org/10.1038/s41598-020-](https://doi.org/10.1038/s41598-020-57678-4)  
505 [57678-4](https://doi.org/10.1038/s41598-020-57678-4)

506 Griffin, D., Zhao, X., McLinden, C. A., Boersma, K. F., Bourassa, A., Dammers, E., et al.  
507 (2019). High-Resolution Mapping of Nitrogen Dioxide With TROPOMI: First Results and  
508 Validation Over the Canadian Oil Sands. *Geophysical Research Letters*, 46(2), 1049–1060.  
509 <https://doi.org/10.1029/2018GL081095>

510 He, H., Hembeck, L., Hosley, K. M., Canty, T. P., Salawitch, R. J., & Dickerson, R. R. (2013).  
511 High ozone concentrations on hot days: The role of electric power demand and NO<sub>x</sub>  
512 emissions. *Geophysical Research Letters*, 40(19), 5291–5294.  
513 <https://doi.org/10.1002/grl.50967>

514 Herman, J., Abuhassan, N., Kim, J., Kim, J., Dubey, M., Raponi, M., & Tzortziou, M. (2019).  
515 Underestimation of column NO<sub>2</sub> amounts from the OMI satellite compared to diurnally  
516 varying ground-based retrievals from multiple PANDORA spectrometer instruments.  
517 *Atmospheric Measurement Techniques*, 12(10), 5593–5612. [https://doi.org/10.5194/amt-12-](https://doi.org/10.5194/amt-12-5593-2019)  
518 [5593-2019](https://doi.org/10.5194/amt-12-5593-2019)

519 Heue, K.-P., Richter, A., Bruns, M., Burrows, J. P., Friedeburg, C. V., Platt, U., et al. (2005).  
520 Validation of SCIAMACHY tropospheric NO<sub>2</sub> columns with AMAXDOAS measurements.  
521 *Atmospheric Chemistry and Physics*, 5, 1039–1051. Retrieved from [www.atmos-chem-](http://www.atmos-chem-phys.org/acp/5/1039/SRef-ID:1680-7324/acp/2005-5-1039)  
522 [phys.org/acp/5/1039/SRef-ID:1680-7324/acp/2005-5-1039](http://www.atmos-chem-phys.org/acp/5/1039/SRef-ID:1680-7324/acp/2005-5-1039)EuropeanGeosciencesUnion

523 Ialongo, I., Herman, J. R., Krotkov, N., Lamsal, L. N., Folkert Boersma, K., Hovila, J., &  
524 Tamminen, J. (2016). Comparison of OMI NO<sub>2</sub> observations and their seasonal and weekly  
525 cycles with ground-based measurements in Helsinki. *Atmospheric Measurement*  
526 *Techniques*, 9(10), 5203–5212. <https://doi.org/10.5194/amt-9-5203-2016>

527 Ialongo, I., Virta, H., Eskes, H., Hovila, J., & Douros, J. (2020). Comparison of  
528 TROPOMI/Sentinel-5 Precursor NO<sub>2</sub> observations with ground-based measurements in  
529 Helsinki. *Atmospheric Measurement Techniques*, 13(1), 205–218.  
530 <https://doi.org/10.5194/amt-13-205-2020>

531 Jacob, D. J. (2000). Heterogeneous chemistry and tropospheric ozone. *Atmospheric*  
532 *Environment*, 34(12–14), 2131–2159. [https://doi.org/10.1016/S1352-2310\(99\)00462-8](https://doi.org/10.1016/S1352-2310(99)00462-8)

533 Judd, L. M., Al-Saadi, J. A., Janz, S. J., Kowalewski, M. G., Pierce, R. B., Szykman, J. J., et al.  
534 (2019). Evaluating the impact of spatial resolution on tropospheric NO<sub>2</sub> column  
535 comparisons within urban areas using high-resolution airborne data. *Atmos. Meas. Tech*, 12,

536 6091–6111. <https://doi.org/10.5194/amt-12-6091-2019>

537 Judd, L. M., Al-Saadi, J. A., Szykman, J. J., Valin, L. C., Janz, S. J., Kowalewski, M. G., et al.  
538 (2020). Evaluating Sentinel-5P TROPOMI tropospheric NO<sub>2</sub> column densities with  
539 airborne and Pandora spectrometers near New York City and Long Island Sound. *AMTD*.  
540 <https://doi.org/10.5194/amt-2020-151>

541 Kleipool, Q. L., Dobber, M. R., de Haan, J. F., & Levelt, P. F. (2008). Earth surface reflectance  
542 climatology from 3 years of OMI data. *Journal of Geophysical Research Atmospheres*,  
543 *113*(18), 1–22. <https://doi.org/10.1029/2008JD010290>

544 Knepp, T., Pippin, M., Crawford, J., Chen, G., Szykman, J., Long, R. W., et al. (2015).  
545 Estimating surface NO<sub>2</sub> and SO<sub>2</sub> mixing ratios from fast-response total column  
546 observations and potential application to geostationary missions. *Journal of Atmospheric*  
547 *Chemistry*, *72*(3–4), 261–286. <https://doi.org/10.1007/s10874-013-9257-6>

548 Konovalov, I. B., Berezin, E. V., Ciais, P., Broquet, G., Zhuravlev, R. V., & Janssens-Maenhout,  
549 G. (2016). Estimation of fossil-fuel CO<sub>2</sub> emissions using satellite measurements of “proxy”  
550 species. *Atmospheric Chemistry and Physics*, *16*(21), 13509–13540.  
551 <https://doi.org/10.5194/acp-16-13509-2016>

552 Krotkov, N. A., McLinden, C. A., Li, C., Lamsal, L. N., Celarier, E. A., Marchenko, S. V., et al.  
553 (2016). Aura OMI observations of regional SO<sub>2</sub> and NO<sub>2</sub> pollution changes from 2005 to  
554 2015. *Atmospheric Chemistry and Physics*, *16*(7), 4605–4629. [https://doi.org/10.5194/acp-](https://doi.org/10.5194/acp-16-4605-2016)  
555 [16-4605-2016](https://doi.org/10.5194/acp-16-4605-2016)

556 Krotkov, N. A., Lamsal, L. N., Celarier, E. A., Swartz, W. H., Marchenko, S. V., Bucsela, E. J.,  
557 et al. (2017). The version 3 OMI NO<sub>2</sub> standard product. *Atmospheric Measurement*  
558 *Techniques*, *10*(9), 3133–3149. <https://doi.org/10.5194/amt-10-3133-2017>

559 Lama, S., Houweling, S., Folkert Boersma, K., Aben, I., Denier Van Der Gon, H. A. C., Krol, M.  
560 C., et al. (n.d.). Quantifying burning efficiency in Megacities using NO<sub>2</sub>/CO ratio from the  
561 Tropospheric Monitoring Instrument (TROPOMI). *ACPD*. [https://doi.org/10.5194/acp-](https://doi.org/10.5194/acp-2019-1112)  
562 [2019-1112](https://doi.org/10.5194/acp-2019-1112)

563 Lamsal, L. N., Martin, R. V., van Donkelaar, A., Steinbacher, M., Celarier, E. A., Bucsela, E., et  
564 al. (2008). Ground-level nitrogen dioxide concentrations inferred from the satellite-borne  
565 Ozone Monitoring Instrument. *Journal of Geophysical Research Atmospheres*, *113*(16), 1–  
566 15. <https://doi.org/10.1029/2007JD009235>

567 Larkin, A., Geddes, J. A., Martin, R. V., Xiao, Q., Liu, Y., Marshall, J. D., et al. (2017). Global  
568 Land Use Regression Model for Nitrogen Dioxide Air Pollution. *Environmental Science*  
569 *and Technology*, *51*(12), 6957–6964. <https://doi.org/10.1021/acs.est.7b01148>

570 Laughner, J. L., & Cohen, R. C. (2019). Direct observation of changing NO<sub>x</sub> lifetime in North  
571 American cities. *Science*, *366*(6466), 723–727. <https://doi.org/10.1126/science.aax6832>

572 Laughner, J. L., Zare, A., & Cohen, R. C. (2016). Effects of daily meteorology on the  
573 interpretation of space-based remote sensing of NO<sub>2</sub>. *Atmospheric Chemistry and Physics*,  
574 *16*(23), 15247–15264. <https://doi.org/10.5194/acp-16-15247-2016>

575 Laughner, J. L., Zhu, Q., & Cohen, R. C. (2019). Evaluation of version 3.0B of the BEHR OMI

- 576 NO<sub>2</sub> product. *Atmospheric Measurement Techniques*, 12(1), 129–146.  
577 <https://doi.org/10.5194/amt-12-129-2019>
- 578 Levelt, P. F., Oord, G. H. J. Van Den, Dobber, M. R., Dirksen, R. J., MÄLKKI, A., VISSER, H.,  
579 et al. (2006). The ozone monitoring instrument. *Ieee Transactions on Geoscience and*  
580 *Remote Sensing*, 44(5), 1093–1101. <https://doi.org/urn:nbn:nl:ui:25-648485>
- 581 Levelt, P. F., Joiner, J., Tamminen, J., Veefkind, J. P., Bhartia, P. K., Zweers, D. C. S., et al.  
582 (2018). The Ozone Monitoring Instrument: Overview of 14 years in space. *Atmospheric*  
583 *Chemistry and Physics*, 18(8), 5699–5745. <https://doi.org/10.5194/acp-18-5699-2018>
- 584 Lin, J. T., Liu, M. Y., Xin, J. Y., Boersma, K. F., Spurr, R., Martin, R. V., & Zhang, Q. (2015).  
585 Influence of aerosols and surface reflectance on satellite NO<sub>2</sub> retrieval: Seasonal and spatial  
586 characteristics and implications for NO<sub>x</sub> emission constraints. *Atmospheric Chemistry and*  
587 *Physics*, 15(19), 11217–11241. <https://doi.org/10.5194/acp-15-11217-2015>
- 588 Liu, F., Page, A., Strode, S. A., Yoshida, Y., Choi, S., Zheng, B., et al. (2020). Abrupt declines  
589 in tropospheric nitrogen dioxide over China after the outbreak of COVID-19. Retrieved  
590 from <http://arxiv.org/abs/2004.06542>
- 591 Liu, M., Lin, J., Boersma, K. F., Pinardi, G., Wang, Y., Chimot, J., et al. (2019). Improved  
592 aerosol correction for OMI tropospheric NO<sub>2</sub> retrieval over East Asia: constraint from  
593 CALIOP aerosol vertical profile. *Atmospheric Measurement Techniques*, 12(1), 1–21.  
594 <https://doi.org/10.5194/amt-12-1-2019>
- 595 Lorente, A., Folkert Boersma, K., Yu, H., Dörner, S., Hilboll, A., Richter, A., et al. (2017).  
596 Structural uncertainty in air mass factor calculation for NO<sub>2</sub> and HCHO satellite retrievals.  
597 *Atmospheric Measurement Techniques*, 10(3), 759–782. [https://doi.org/10.5194/amt-10-](https://doi.org/10.5194/amt-10-759-2017)  
598 [759-2017](https://doi.org/10.5194/amt-10-759-2017)
- 599 Lorente, A., Boersma, K. F., Eskes, H. J., Veefkind, J. P., van Geffen, J. H. G. M., de Zeeuw, M.  
600 B., et al. (2019). Quantification of nitrogen oxides emissions from build-up of pollution  
601 over Paris with TROPOMI. *Scientific Reports*, 9(1), 20033. [https://doi.org/10.1038/s41598-](https://doi.org/10.1038/s41598-019-56428-5)  
602 [019-56428-5](https://doi.org/10.1038/s41598-019-56428-5)
- 603 Lu, Z., Streets, D. G., de Foy, B., Lamsal, L. N., Duncan, B. N., & Xing, J. (2015). Emissions of  
604 nitrogen oxides from US urban areas: Estimation from Ozone Monitoring Instrument  
605 retrievals for 2005-2014. *Atmospheric Chemistry and Physics*, 15(18), 10367–10383.  
606 <https://doi.org/10.5194/acp-15-10367-2015>
- 607 Ma, J. Z., Beirle, S., Jin, J. L., Shaiganfar, R., Yan, P., & Wagner, T. (2013). Tropospheric NO<sub>2</sub>  
608 vertical column densities over Beijing: Results of the first three years of ground-based  
609 MAX-DOAS measurements (2008-2011) and satellite validation. *Atmospheric Chemistry*  
610 *and Physics*, 13(3), 1547–1567. <https://doi.org/10.5194/acp-13-1547-2013>
- 611 Martin, R. V., Chance, K., Jacob, D. J., Kurosu, T. P., Spurr, R. J. D., Bucsela, E., et al. (2002).  
612 An improved retrieval of tropospheric nitrogen dioxide from GOME. *Journal of*  
613 *Geophysical Research D: Atmospheres*, 107(20). <https://doi.org/10.1029/2001JD001027>
- 614 McConnell, R., Berhane, K., Gilliland, F., London, S. J., Islam, T., Gauderman, W. J., et al.  
615 (2002). Asthma in exercising children exposed to ozone: a cohort study. *Lancet (London,*

616 *England*), 359(9304), 386–91. [https://doi.org/10.1016/S0140-6736\(02\)07597-9](https://doi.org/10.1016/S0140-6736(02)07597-9)

617 McLinden, C. A., Fioletov, V. E., Krotkov, N. A., Li, C., Boersma, K. F., & Adams, C. (2016).  
618 A Decade of Change in NO<sub>2</sub> and SO<sub>2</sub> over the Canadian Oil Sands As Seen from Space.  
619 *Environmental Science and Technology*, 50(1), 331–337.  
620 <https://doi.org/10.1021/acs.est.5b04985>

621 Munro, R., Lang, R., Klaes, D., Poli, G., Retscher, C., Lindstrot, R., et al. (2016). The GOME-2  
622 instrument on the Metop series of satellites: instrument design, calibration, and level 1 data  
623 processing – an overview. *Atmospheric Measurement Techniques*, 9(3), 1279–1301.  
624 <https://doi.org/10.5194/amt-9-1279-2016>

625 Penn, E., & Holloway, T. (2020). Evaluating current satellite capability to observe diurnal  
626 change in nitrogen oxides in preparation for geostationary satellite missions. *Environmental*  
627 *Research Letters*. <https://doi.org/10.1088/1748-9326/ab6b36>

628 Qu, Z., Henze, D. K., Capps, S. L., Wang, Y., Xu, X., Wang, J., & Keller, M. (2017). Monthly  
629 top-down NO<sub>x</sub> emissions for China (2005–2012): A hybrid inversion method and trend  
630 analysis. *Journal of Geophysical Research*, 122(8), 4600–4625.  
631 <https://doi.org/10.1002/2016JD025852>

632 Rasool, Q. Z., Bash, J. O., & Cohan, D. S. (2019). Mechanistic representation of soil nitrogen  
633 emissions in the Community Multiscale Air Quality (CMAQ) model v 5.1. *Geosci. Model*  
634 *Dev*, 12, 849–878. <https://doi.org/10.5194/gmd-12-849-2019>

635 Reuter, M., Buchwitz, M., Schneising, O., Krautwurst, S., O'dell, C. W., Richter, A., et al.  
636 (2019). Towards monitoring localized CO<sub>2</sub> emissions from space: co-located regional CO<sub>2</sub>  
637 and NO<sub>2</sub> enhancements observed by the OCO-2 and S5P satellites. *Atmospheric Chemistry*  
638 *and Physics*, 19, 9371–9383. <https://doi.org/10.5194/acp-19-9371-2019>

639 Richter, A., & Burrows, J. P. (2002). *TROPOSPHERIC NO<sub>2</sub> FROM GOME MEASUREMENTS*.  
640 *Adv. Space Res* (Vol. 29). Retrieved from [www.elsevier.com/locate/asr](http://www.elsevier.com/locate/asr)

641 Richter, A., Begoin, M., Hilboll, A., & Burrows, J. P. (2011). An improved NO<sub>2</sub> retrieval for the  
642 GOME-2 satellite instrument. *Atmospheric Measurement Techniques*, 4(6), 1147–1159.  
643 <https://doi.org/10.5194/amt-4-1147-2011>

644 Romer, P. S., Duffey, K. C., Wooldridge, P. J., Edgerton, E., Baumann, K., Feiner, P. A., et al.  
645 (2018). Effects of temperature-dependent NO<sub>x</sub> emissions on continental ozone production.  
646 *Atmospheric Chemistry and Physics*, 18(4), 2601–2614. <https://doi.org/10.5194/acp-18-2601-2018>

648 Russell, A. R., Valin, L. C., Bucsela, E. J., Wenig, M. O., & Cohen, R. C. (2010). Space-based  
649 constraints on spatial and temporal patterns of NO<sub>x</sub> emissions in California, 2005–2008.  
650 *Environmental Science and Technology*, 44(9), 3608–3615.  
651 <https://doi.org/10.1021/es903451j>

652 Russell, A. R., Perring, A. E., Valin, L. C., Bucsela, E. J., Browne, E. C., Wooldridge, P. J., &  
653 Cohen, R. C. (2011). A high spatial resolution retrieval of NO<sub>2</sub> column densities from OMI:  
654 Method and evaluation. *Atmospheric Chemistry and Physics*, 11(16), 8543–8554.  
655 <https://doi.org/10.5194/acp-11-8543-2011>

- 656 Shah, V., Jacob, D. J., Li, K., Silvern, R. F., Zhai, S., Liu, M., et al. (2020). Effect of changing  
657 NO<sub>x</sub> lifetime on the seasonality and long-term trends of satellite-observed tropospheric  
658 NO<sub>2</sub> columns over China. *Atmospheric Chemistry and Physics Discussions*, 20(3), 1483–  
659 1495. <https://doi.org/10.5194/acp-2019-670>
- 660 Sourì, A. H., Choi, Y., Jeon, W., Li, X., Pan, S., Diao, L., & Westenbarger, D. A. (2016).  
661 Constraining NO<sub>x</sub> emissions using satellite NO<sub>2</sub> measurements during 2013 DISCOVER-  
662 AQ Texas campaign. *Atmospheric Environment*, 131(2), 371–381.  
663 <https://doi.org/10.1016/j.atmosenv.2016.02.020>
- 664 Stavrakou, T., Müller, J.-F., Boersma, K. F., De Smedt, I., & van der A, R. J. (2008). Assessing  
665 the distribution and growth rates of NO<sub>x</sub> emission sources by inverting a 10-year record of  
666 NO<sub>2</sub> satellite columns. *Geophysical Research Letters*, 35(10).  
667 <https://doi.org/10.1029/2008GL033521>
- 668 Timmermans, R., Segers, A., Curier, L., Abida, R., Attié, J.-L., El Amraoui, L., et al. (2019).  
669 Impact of synthetic space-borne NO<sub>2</sub> observations from the Sentinel-4 and Sentinel-5P  
670 missions on tropospheric NO<sub>2</sub> analyses. *Atmospheric Chemistry and Physics*, 19(19),  
671 12811–12833. <https://doi.org/10.5194/acp-19-12811-2019>
- 672 Tzortziou, M. A., Herman, J. R., Cede, A., Loughner, C. P., Abuhassan, N. K., & Naik, S.  
673 (2015). Spatial and temporal variability of ozone and nitrogen dioxide over a major urban  
674 estuarine ecosystem. *Journal of Atmospheric Chemistry*, 72(3–4), 287–309.  
675 <https://doi.org/10.1007/s10874-013-9255-8>
- 676 Valin, L. C., Russell, A. R., Hudman, R. C., & Cohen, R. C. (2011). Effects of model resolution  
677 on the interpretation of satellite NO<sub>2</sub> observations. *Atmospheric Chemistry and Physics*,  
678 11(22), 11647–11655. <https://doi.org/10.5194/acp-11-11647-2011>
- 679 Valin, L. C., Russell, A. R., & Cohen, R. C. (2013). Variations of OH radical in an urban plume  
680 inferred from NO<sub>2</sub> column measurements. *Geophysical Research Letters*, 40(9), 1856–  
681 1860. <https://doi.org/10.1002/grl.50267>
- 682 Valin, L. C., Russell, A. R., & Cohen, R. C. (2014). Chemical feedback effects on the spatial  
683 patterns of the NO<sub>x</sub> weekend effect: A sensitivity analysis. *Atmospheric Chemistry and*  
684 *Physics*, 14(1), 1–9. <https://doi.org/10.5194/acp-14-1-2014>
- 685 Vandaele, A. C., Hermans, C., Simon, P. C., Carleer, M., Colin, R., Fally, S., et al. (1998).  
686 Measurements of the NO<sub>2</sub> absorption cross-section from 42 000 cm<sup>-1</sup> to 10 000 cm<sup>-1</sup>  
687 (238–1000 nm) at 220 K and 294 K. *Journal of Quantitative Spectroscopy and Radiative*  
688 *Transfer*, 59(3–5), 171–184. [https://doi.org/10.1016/S0022-4073\(97\)00168-4](https://doi.org/10.1016/S0022-4073(97)00168-4)
- 689 VanDerA, R. J., Eskes, H. J., Boersma, K. F., van Noije, T. P. C., Van Roozendaal, M., De  
690 Smedt, I., et al. (2008). Trends, seasonal variability and dominant NO<sub>x</sub> source derived from  
691 a ten year record of NO<sub>2</sub> measured from space. *Journal of Geophysical Research*  
692 *Atmospheres*, 113(4), 1–12. <https://doi.org/10.1029/2007JD009021>
- 693 VanDonkelaar, A., Martin, R. V., Li, C., & Burnett, R. T. (2019). Regional Estimates of  
694 Chemical Composition of Fine Particulate Matter using a Combined Geoscience-Statistical  
695 Method with Information from Satellites, Models, and Monitors. *Environmental Science &*  
696 *Technology*, acs.est.8b06392. <https://doi.org/10.1021/acs.est.8b06392>

697 VanGeffen, J. H. G. M., Eskes, H. J., Boersma, K. F., Maasakkers, J. D., & Veefkind, J. P.  
698 (2019). *TROPOMI ATBD of the total and tropospheric NO2 data products*. Retrieved from  
699 <http://www.tropomi.eu/sites/default/files/files/publicS5P-KNMI-L2-0005-RP->  
700 [ATBD\\_NO2\\_data\\_products-20190206\\_v140.pdf](http://www.tropomi.eu/sites/default/files/files/publicS5P-KNMI-L2-0005-RP-ATBD_NO2_data_products-20190206_v140.pdf)

701 Veefkind, J. P., Aben, I., McMullan, K., Förster, H., de Vries, J., Otter, G., et al. (2012).  
702 TROPOMI on the ESA Sentinel-5 Precursor: A GMES mission for global observations of  
703 the atmospheric composition for climate, air quality and ozone layer applications. *Remote*  
704 *Sensing of Environment*, 120(2012), 70–83. <https://doi.org/10.1016/j.rse.2011.09.027>

705 Wang, Y., Bechle, M. J., Kim, S.-Y., Adams, P. J., Pandis, S. N., Pope, C. A., et al. (2020).  
706 Spatial decomposition analysis of NO2 and PM2.5 air pollution in the United States.  
707 *Atmospheric Environment*, 117470. <https://doi.org/10.1016/j.atmosenv.2020.117470>

708 Zhao, X., Griffin, D., Fioletov, V., McLinden, C. A., Cede, A., Tiefengraber, M., et al. (2020).  
709 Assessment of the quality of TROPOMI high-spatial-resolution NO2 data products in the  
710 Greater Toronto Area. *Atmospheric Measurement Techniques*, 13(4), 2131–2159.  
711 <https://doi.org/10.5194/amt-13-2131-2020>

712 Zoogman, P., Liu, X., Suleiman, R. M., Pennington, W. F., Flittner, D. E., Al-Saadi, J. A., et al.  
713 (2017). Tropospheric emissions: Monitoring of pollution (TEMPO). *Journal of Quantitative*  
714 *Spectroscopy and Radiative Transfer*, 186(2017), 17–39.  
715 <https://doi.org/10.1016/j.jqsrt.2016.05.008>

716